Since January 2020 Elsevier has created a COVID-19 resource centre with free information in English and Mandarin on the novel coronavirus COVID-19. The COVID-19 resource centre is hosted on Elsevier Connect, the company's public news and information website.

Spectrochimica Acta Part A: Molecular and Biomolecular Spectroscopy 244 (2021) 118825

Contents lists available at ScienceDirect

Spectrochimica Acta Part A: Molecular and Biomolecular Spectroscopy

journal homepage: www.elsevier.com/locate/saa

Quantum chemical insight into molecular structure, NBO analysis of the hydrogen-bonded interactions, spectroscopic (FT–IR, FT–Raman), drug likeness and molecular docking of the novel anti COVID-19 molecule 2-[(4,6-diaminopyrimidin-2-yl)sulfanyl]-N-(4-fluorophenyl)acetamide - dimer

S.J. Jenepha Mary [a], Mohd Usman Mohd Siddique [b,d], Sayantan Pradhan [c], Venkatesan Jayaprakash [d], C. James [a,*]

[a] Register number 18113162132001, Department of Physics and Research Centre, Scott Christian College (Autonomous), Nagercoil- 629003, Tamil Nadu, Affiliated to Manonmaniam Sundarnar University, Abishekapatti, Tirunelveli 627012, India
[b] Department of Pharmaceutical Chemistry, Shri Vile Parle Kelavani Mandal's Institute of Pharmacy, Dhule, Maharashtra 424001, India
[c] Department of Chemistry, Jadavpur University, Kolkata 700 032, WestBengal, India.
[d] Department of Pharmaceutical Sciences & Technology, Birla Institute of Technology, Mesra, Ranchi 835215, JH, India

ARTICLE INFO

Article history:
Received 29 May 2020
Received in revised form 15 July 2020
Accepted 20 July 2020
Available online 12 August 2020

Keywords:
Density functional theory
Natural bond orbital analysis
Hirshfeld surface
FT-IR and Raman spectra
SARS-CoV-2

ABSTRACT

Novel antiviral active molecule 2- [(4,6-diaminopyrimidin-2-yl)sulfanyl]-N-(4-fluoro- phenyl)acetamide has been synthesised and characterized by FT-IR and FT-Raman spectra. The equilibrium geometry, natural bond orbital calculations and vibrational assignments have been carried out using density functional B3LYP method with the 6-311G++(d,p) basis set. The complete vibrational assignments for all the vibrational modes have been supported by normal coordinate analysis, force constants and potential energy distributions. A detailed analysis of the intermolecular interactions has been performed based on the Hirshfeld surfaces. Drug likeness has been carried out based on Lipinski's rule and the absorption, distribution, metabolism, excretion and toxicity of the title molecule has been calculated. Antiviral potency of 2- [(4,6-diaminopyrimidin-2-yl)sulfanyl]-N-(4-fluoro-phenyl) acetamide has been investigated by docking against SARS-CoV-2 protein. The optimized geometry shows near-planarity between the phenyl ring and the pyrimidine ring. Differences in the geometries due to the substitution of the most electronegative fluorine atom and intermolecular contacts due to amino pyrimidine were analyzed. NBO analysis reveals the formation of two strong stable hydrogen bonded N–H···N intermolecular interactions and weak intramolecular interactions C–H···O and N–H···O. The Hirshfeld surfaces and consequently the 2D-fingerprint confirm the nature of intermolecular interactions and their quantitative contributions towards the crystal packing. The red shift in N–H stretching frequency exposed from IR substantiate the formation of N–H···N intermolecular hydrogen bond. Drug likeness and absorption, distribution, metabolism, excretion and toxicity properties analysis gives an idea about the pharmacokinetic properties of the title molecule. The binding energy −8.7 kcal/mol of the nonbonding interaction present a clear view that 2- [(4,6-diaminopyrimidin-2-yl)sulfanyl]-N-(4-fluoro- phenyl) acetamide can irreversibly interact with SARS-CoV-2 protease.

1. Introduction

Pyrimidine and its derivatives take up a key position in the field of medicinal chemistry due to its multifarious pharmacological activities. In an urge for searching new promising small therapeutic agents, we introduce 2- [(4,6-diaminopyrimidin-2-yl)sulfanyl]-N-(4-fluoro- phenyl) acetamide (DAPF). In the present study, we focus on the investigation on the molecular structure, electronic properties, vibrational spectra and molecular docking of the title compound, with the hope that the results of the present investigation may be decisive in the prognosis of its mechanism of biological activity.

Pyrimidines, the fundamental building blocks for nucleic acids, are invoking much scientific interest owing to their potential biological activities and pharmacological applications [1]. Pyrimidines are also reported to show anti-HIV, [2] antidengue [3] and anticancer [4] activities. The title compound DAPF, which has the amino substituent at the 4,6- position are found to be Troponin I-Interacting Kinase

* Corresponding author.
E-mail address: james@scottchristian.org (C. James).

https://doi.org/10.1016/j.saa.2020.118825
1386-1425/

(TNNI3K) Inhibitors [5]. Also, the presence of the amino group in the 4-position are found to be HIV inhibitors [6]. Aminopyrimidines and polyaminopyrimidines are important therapeutic agents used as tyrosine kinase inhibitor such as Gleevec and the hypocholesterolemic agent rosuvastatin [7–9].

Molecular and spectral investigation of 2-mercapto pyrimidine and 2,4-diamino-6-hydroxy-5-nitroso pyrimidine [10], pyrazinamide [11], DFT assisted Quantum computations of aminopyrimidine [12], 2-amino-5-nitropyrimidines [13], FT-IR spectral study on 4-aminopyrimidine and deuterium substituted 4-aminopyrimidine [13], fluocytosine [14] have been carried out and the vibrational bands have been reported. The C—S stretching frequencies in sulfanyl-aminobenzene have been reported [15]. The nature of substituent at 2- and 6-positions in the pyrimidine ring was found to greatly influence the anti-tubercular activity. Structural study by spectroscopic and quantum chemical methods, have been reported on chloropyrimidine based anti-microbial agents such as 4-cholro2,6-dimethylsulfanyl pyrimidine-5-carbonitrile and 4-cholro-2- methylsulfanyl-6-(2-thienyl) pyrimidine-5-carbonitrile which demonstrates activity against M. Tuberculosis [16]. The title molecule has gained attention owing to its structure, functional group and their diverse biological activity. Crystal structure of the title compound [17] has been reported and no other studies have been reported so far. The initiation of cART (combinational antiretroviral therapy) drugs ritonavir, darunavir, and lamivudine/zidovudine did not reduce the cerebellar dysfunctions such as ataxia, dementia and neurocognitive disorders associated with HIV infections. The presence of the amino group in the title molecule has the ability to reduce the cerebellar dysfunction [18]. The physical, biochemical, pharmacological and pharmacokinetic properties of fluorine atom in the title molecules may play an important role in drug design owing to their C—F bond strength, dipole moment, strong electronegetivity and modest lipophilicity [19].

Elucidating the structure activity of DAPF using density functional theory, spectroscopic techniques and molecular docking may pave a way in the development of new HIV protease inhibitor which may reduce the cerebellar dysfunctions. Even though DFT studies have been reported on pyrimidine derivatives, spectral investigation and density functional theory studies of DAPF has not been carried out.

Vibrational spectral analysis of DAPF using quantum chemical computations aided by density functional theory is an efficient method in understanding the various types of bonding and normal modes of vibrations. The complete vibrational assignments for all the vibrational modes have been supported by normal coordinate analysis, force constants and potential energy distributions. A detailed analysis of the intermolecular interactions has been performed using NBO analysis and the intermolecular contacts have been exposed based on the Hirshfeld surface analysis. Antiviral potency of DAPF has been investigated by docking against viral proteins.

The theoretical and experimental calculations have been carried out to probe the structure of DAPF. Also, FT-IR and FT-Raman spectra of DAPF have been described by both experimental and theoretical methods. The antiviral activity has been performed using molecular docking studies, which shows it can irreversibly interact with SARS-CoV-2 main protease.

2. Experimental

To an ethanolic solution of 4,6-diamino-pyrimidine-2- thiol (0.5 g, 3.52 mmol) potassium hydroxide (0.2 g, 3.52 mmol) was added and the mixture was refluxed for 30 min. To this 3.52 mmol of 2-chloro-N-(4-fluoro- phenyl) acetamide was added and the mixture was refluxed for 4 h. The completion of the reaction has been monitored by thin layer chromatography (TLC). Ethanol was evaporated *in vacuo* and cold water was added and the precipitate formed was filtered and dried to give a crystalline powder. Colourless block-like crystals were obtained by slow evaporation [17].

The room temperature FTIR spectra of the compound was measured in the 4000–400 cm1 region at a resolution of š1 cm1 using a BRUKER IFS-66*V* vacuum Fourier transform spectrometer equipped with a mercury cadmium telluride (MCT) detector, a KBr beam splitter and globar source. The far IR spectrum was recorded on the same instrument using the polyethylene pellet technique.

The mid-infrared spectrum of the sample has been recorded in the region 4000–400 cm^{-1} at a resolution of 1 cm^{-1} using a PerkinElmer Spectrum1 FT-IR spectrophotometer, with the samples in the form of KBr pellets. The FT-Raman spectrum has been recorded using Bruker RFS 27 spectrometer in the region 4000–50 cm^{-1} with the use of Nd: YAG 1064 nm laser source.

3. Computational details

The equilibrium geometry and the vibrational wavenumbers of the title molecule has been done using Gaussian 09W [20] program package. The geometric optimization has been carried out using DFT calculations at the B3LYP/6-311G++(d,p) level of theory. The natural bonding orbitals (NBO) calculations [21] have been carried out using NBO3.1 program as implemented in the Gaussian 09W package at the DFT/B3LYP level in order to understand the interactions that takes place between the filled and vacant orbitals, which is a measure of delocalization or hyperconjugation. The normal coordinate analysis (NCA) has been performed using MOLVIB 7.0 program [22,23]. The input for the MOLVIB program has been given as suggested by Pulay [24]. Crystal Explorer program 3.1.0 has been employed to carry out the Hirshfeld surface [25] and the associated 2D-fingerprint plots [26]. Molecular docking simulation has been carried out using the Auto Dock 4.2.6 software package and the ligand-protein interactions have been studied [27]. The ligand-protein binding sites have been visualized using PYMOL graphic software [28].

4. Result and discussions

4.1. Optimized geometry

The optimized structural parameters of the monomer and dimer form of the title compound have been performed using GAUSSIAN 09W program package and the optimized structure has been visualized using Gauss View 5.0.9. Geometric optimization has been carried out using B3LYP function and 6-311G++(d,p) basis set. The optimized dimer structure of the DAPF is depicted in Fig. 1.

The optimized bond length of DAPF is given in Table 1. The optimized bond angle and dihedral angle of DAPF have been shown in Tables S2 and S3.

The molecular structure and the crystallographic information of DAPF [$C_{12}H_{12}FN_5OS$] have been taken from Cambridge Crystallographic Data Center (CCDC 1529607). The molecular structure of DAPF constitutes a di substituted phenyl ring and a tri substituted pyrimidine ring bridged by thioacetamide moiety. The observed theoretical parameters are in good agreement with the experimental data with certain discrepancies. The C2– C3, C3– C4 bond lengths in the phenyl ring are shortened when compared to other C—C bond length and the endoangle C2-C3– C4 (121.56°) has been increased, leading to the distortion from the regular hexagon structure, due to the substitution of the most electronegative fluorine atom. There exist an intramolecular interaction between N12– H13 of the sulfanylacetamide moiety and the nitrogen atom N25 of the pyrimidine ring resulting in an increase of N12– H13 bond length (0.01Å). On dimerization, DAPF leads to the formation of two N–H···N hydrogen bonded intermolecular interactions, which adds stability to the system. This hydrogen bonded interaction causes substantial changes with an increase in the N30– H31 bond length by 0.018 Å and the C22– N30– H31 bond angle by 5° when compared with the single molecular structure. This elongation of N– H bond may be due to charge redistributions and orbital interactions [29].

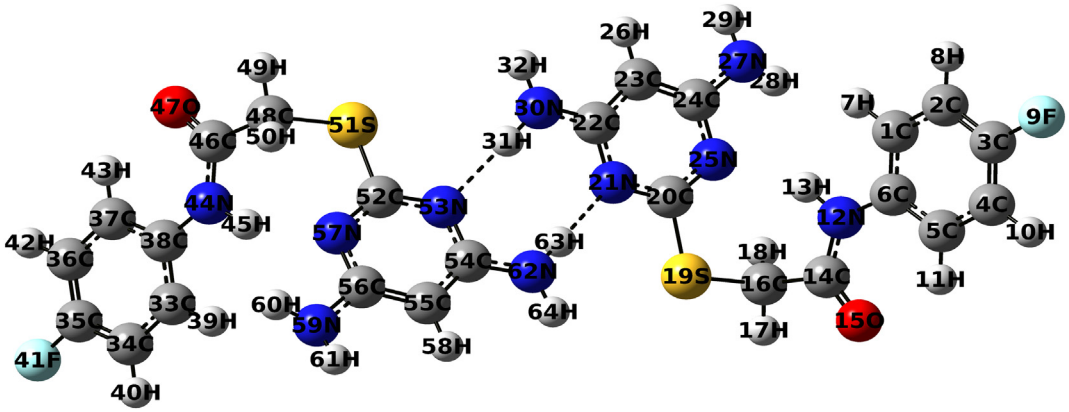

Fig. 1. Optimized molecular structure of DAPF dimer at Becke three Lee–Yang–Parr/6-311++G(d,p) level of theory representing the most stable structure with minimum energy.

4.2. Natural bond orbital study

DAPF has been subjected to NBO analysis to elucidate the possible intramolecular and intermolecular interactions between the filled and vacant orbital, which is a measure of hyperconjugation or intramolecular delocalization. The stabilization energy E(2) associated with the interaction between the filled orbital i and the vacant orbital j, calculated by the second order perturbation theory [30] have been tabulated (Table 2).

Intramolecular interactions arises due to the hyperconjugation and electron density transfer (EDT) from filed lone pair electrons of the n (Y) of the "Lewis base" Y into the unfilled anti-bond σ*(X– Y) of the "Lewis acid" in X-H···Y have been recorded [31]. The calculated second order perturbation energies (E(2)) in NBO basis confirms the presence of a hydrogen bonded intramolecular interactions n1(O25) → σ*(N12– H13) with the stabilization energy of 7.72 kcal/mol. As a result, the length of the N– H bond involved in intramolecular interaction is lengthened by 0.01 Å respectively. This is well reflected in the optimized molecular geometry. The NBO studies on DAPF monomer and dimer manifests the formation of two strong H-bonded intermolecular interactions between the nitrogen lone pairs n1(N30) and σ* (N62–H63) antibonding orbital. The occupancies and their energies for the interacting NBOs are represented in Table 3.

The magnitude of charge transferred from lone pairs of n(N21) → σ* (N62– H63) and n(N53) → σ* (N30– H31) has been significantly

Table 1
Optimized bond length of DAPF monomer and dimer by Becke three Lee–Yang–Parr/6-311G++(d,p) in comparison with X-ray diffraction data.

Bond length	Monomer	Dimer	Δ(d-m)	Expt.
	Calc/Å	Calc/Å	/Å	/Å
C1–C2	1.387	1.387	0.000	1.377
C1–C6	1.401	1.400	−0.001	1.386
C1–H7	1.085	1.085	0.000	0.930
C2–C3	1.384	1.384	0.000	1.358
C2–H8	1.082	1.082	0.000	0.930
C3–C4	1.382	1.382	0.000	1.359
C3–F9	1.353	1.352	−0.001	1.360
C4–C5	1.390	1.390	0.000	1.389
C4–H10	1.083	1.083	0.000	0.930
C5–C6	1.399	1.399	0.000	1.389
C5–H11	1.078	1.078	0.000	0.930
C6–N12	1.407	1.407	0.000	1.415
N12–H13	1.018	1.019	0.001	0.860
N12–C14	1.366	1.365	−0.001	1.339
C14–O15	1.218	1.218	0.000	1.223
C14–C16	1.529	1.529	0.000	1.513
C16–H17	1.087	1.087	0.000	0.970
C16–H18	1.089	1.089	0.000	0.970
C16–S19	1.834	1.833	−0.001	1.805
S19–C20	1.777	1.782	0.005	1.762
C20–N21	1.325	1.326	0.001	1.329
C20–N25	1.331	1.327	−0.004	1.321
N21–C22	1.342	1.354	0.012	1.359
C22–C23	1.400	1.405	0.005	1.388
C22–N30	1.364	1.344	−0.020	1.345
C23–C24	1.389	1.385	−0.004	1.384
C23–H26	1.082	1.082	0.000	0.930
C24–N25	1.350	1.354	0.004	1.361
C24–N27	1.374	1.374	0.000	1.344
N27–H28	1.009	1.009	0.000	0.860
N27–H29	1.008	1.008	0.000	0.860
N30–H31	1.008	1.022	0.014	0.860
N30–H32	1.006	1.005	−0.001	0.860
Inter and intramolecular distances				
N21···H63	–	2.029	2.029	2.291
H31···N53	–	2.024	2.024	2.291
H13···N25	2.034	0.000	−2.034	2.245

Å- Angstrom.
Δ(d-m)- Difference in bond length between dimer and monomer molecule.
Expt - Experimental.

Table 2
Second Order Perturbation Theory Analysis of Fock Matrix of DAPF dimer in NBO basis.

Donor	Acceptor	E(2)	E(j)– E(i)	F(i,j)
(i)	(j)	kcal/mol	a.u	a.u
n3(F9)	π* (C3–C4)	18.17	0.43	0.086
n1(N12)	π* (C5–C 6)	34.89	0.29	0.091
n1(N12)	π* (C14–O15)	63.18	0.28	0.12
n2(O15)	σ* (N12–C14)	25.17	0.72	0.122
n2(O15)	σ* (C5–H11)	1.1	0.73	0.026
n2(O15)	σ* (C14–C16)	21.16	0.61	0.103
n2(S19)	σ* (C14–C16)	5.05	0.61	0.051
n2(S19)	π* (C20–N21)	25.65	0.22	0.073
n1(N21)	σ* (C20–N25)	12.48	0.88	0.095
n1(N21)	σ* (C22–N30)	4.03	0.84	0.053
n1(N25)	σ* (N12–H13)	7.31	0.8	0.069
n1(N25)	σ* (C20–N21)	11.97	0.9	0.094
n1(N25)	σ* (C23–C24)	9.01	0.92	0.083
n1(N27)	π* (C24–N25)	39.71	0.29	0.105
n1(N30)	π* (C22–C23)	58.38	0.26	0.116
From unit1 to unit 2				
n1(N21)	σ* (N62–H63)	10.54	0.8	0.084
From unit2 to unit 1				
n1(N53)	σ* (N30–H31)	10.64	0.8	0.084
Within unit 2				
n1(N53)	σ* (C52 - N57)	12.48	0.88	0.095
n1(N53)	σ* (C54 - C55)	9	0.88	0.081
n1(N53)	σ* (C54 - N62)	4.02	0.84	0.053
n1(N62)	π* (C54 - C55)	59.61	0.26	0.116

E(2) represents energy of the hyperconjugative interaction.
E(j)– E(i) is the energy difference between donor(i) and acceptor(j) NBO orbitals.
F(i,j) is the Fock matrix element between i and j NBO orbitals.

Table 3
Occupancy of the interacting NBOS with their corresponding energies of DAPF monomer and dimer.

Parameters	Occupancy (e)			Energy (a.u.)		
	Monomer	Dimer	Δocc	Monomer	Dimer	Δ
\n1(N21)	1.89501	1.88287	−0.01214	−0.3476	−0.36193	−0.01433
σ* (N30– H31)	0.00837	0.03613	0.02776	0.40416	0.43901	0.03485
σ* (C22– N30)	0.03048	0.02634	−0.00414	0.44296	0.48025	0.03729
σ* (N21– C22)	0.02521	0.02732	0.00211	0.50599	0.48755	−0.01844
n1(N53)	1.89509	1.88303	−0.01206	−0.3476	−0.36232	−0.01472
[a]σ*(C54– C55)	0.03281	0.03087	−0.00194	0.5252	0.52014	−0.00506
[a]σ* (N62– H63)	0.00837	0.03583	0.02746	0.43901	0.43876	−0.00025
[a]σ* (C54– N62)	0.03048	0.02626	−0.00422	0.48025	0.48147	0.00122
σ* (C22– C23)	0.03281	0.03094	−0.00187	0.5252	0.5202	−0.005
n1(N30)	1.78013	1.71749	−0.06264	−0.29972	−0.26689	0.03283

Δocc difference in occupancy between dimer and monomer.
[a] Values for monomer are taken from identical NBOs of other unit.

Table 4
Composition of H-bonded NBOs in terms of natural atomic hybrids of DAPF monomer and dimer.

NBO	Monomer	Dimer	ΔNBO
sp^n (N30–H31)	$sp^{2.69}$	$sp^{2.16}$	−0.053
% s-char	27.040	31.630	4.590
pol. N30%	30.170	27.190	−2.980
pol. H31%	69.830	72.810	2.980
q(N30)/e	0.549	0.521	−0.028
q(H31)/e	−0.836	−0.853	−0.018
sp^n (C22– N30)	$sp^{1.88}$	$sp^{1.87}$	0.01
% s-char	34.650	34.720	0.070
pol. C22%	41.250	40.780	−0.470
pol. N30%	58.750	59.220	0.470
q(C22)/e	0.642	0.639	−0.004
q(N30)/e	−0.767	−0.770	−0.003

increased by 0.02746e and 0.02776e upon dimerization. This evinces the weakening of the bond strength and the elongation of bond length. The hyperconjugative interactions between n1(N21) → σ* (N62– H63) and n1(N53) → σ* (N30–H31) with the stabilization energy of 10.54 kcal/mol quantify the extend of intermolecular interactions.

The effect of rehybridization has a negative impact in N30– H31 bond. The observed data from Table 4 shows that the *s*-character of N30– H31 hybrid orbital has been increased by 4.59% from $sp^{2.60}$ to $sp^{2.16}$ that leads to the strengthening of N30– H31bond and its contraction. The composition of hydrogen bonded natural bonding orbitals in terms of natural atomic hybrids shows that the redistribution of natural charges in the N– H bond becomes negative (−0.0177) at H31 resulting in the destabilization of the H-bond. The effect of rehybridization and hyperconjugation result in the contraction and the elongation of the N — H bond. However the effect of rehybridization has been overcome by the hyperconjugative effect resulting in the elongation of N– H bond and a concomitant red shift in N– H stretching frequency.

4.3. Hirshfeld surface analysis

Hirshfeld surface analysis provides an insight into the intermolecular interactions in the crystal structure because it is not only connected with molecule itself but it has also contributions from nearest neighbour molecules. Hirshfeld surface analysis of DAPF was carried out using Crystal Explorer 3.1 to investigate the short contacts between atoms with potential to form hydrogen bonds and the quantitative ratios of these interactions besides of the π stacking interactions [32–33]. The Hirshfeld surface of DAPF mapped over d_{norm} has been depicted in Fig. 2.

For the 3D Hirshfeld surfaces, 2D view on intermolecular contacts in crystals can be generated by building 2D finger plots [34]. From

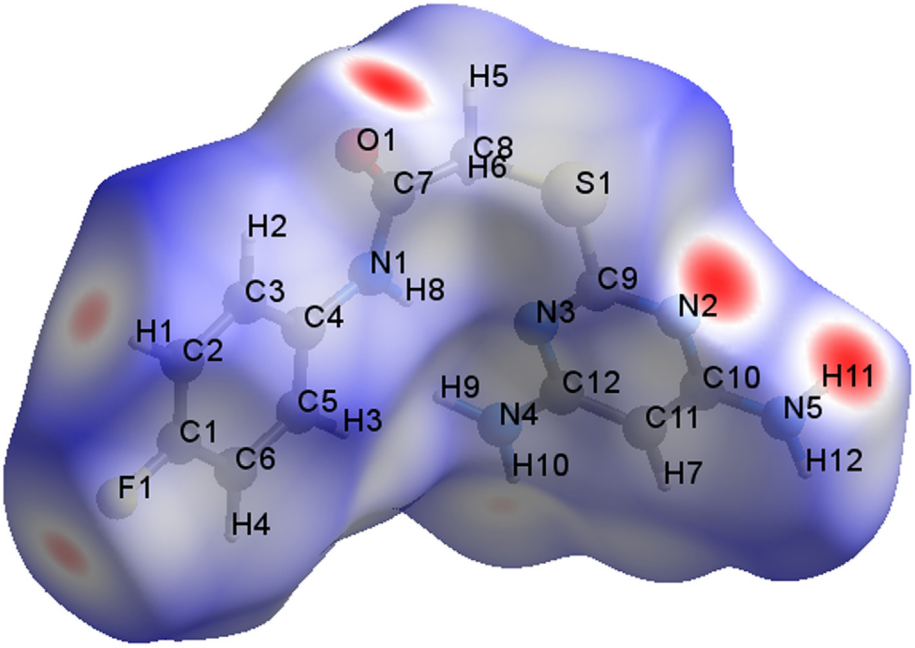

Fig. 2. Hirshfeld surface of DAPF mapped over d_{norm} region −0.382 to +1.154 a.u.

the fingerprint plot Fig. 3(a), the N···H interactions are represented by a spike in the bottom left of the fingerprint plot, whose contribution is 8% and the counterpart H···N interaction is represented on the bottom right of the fingerprint plot with the contribution of 6.6%, of the total N···H/H···N 14.6%. The most prominent N···H interaction is from the hydrogen of the amino group, with the nitrogen

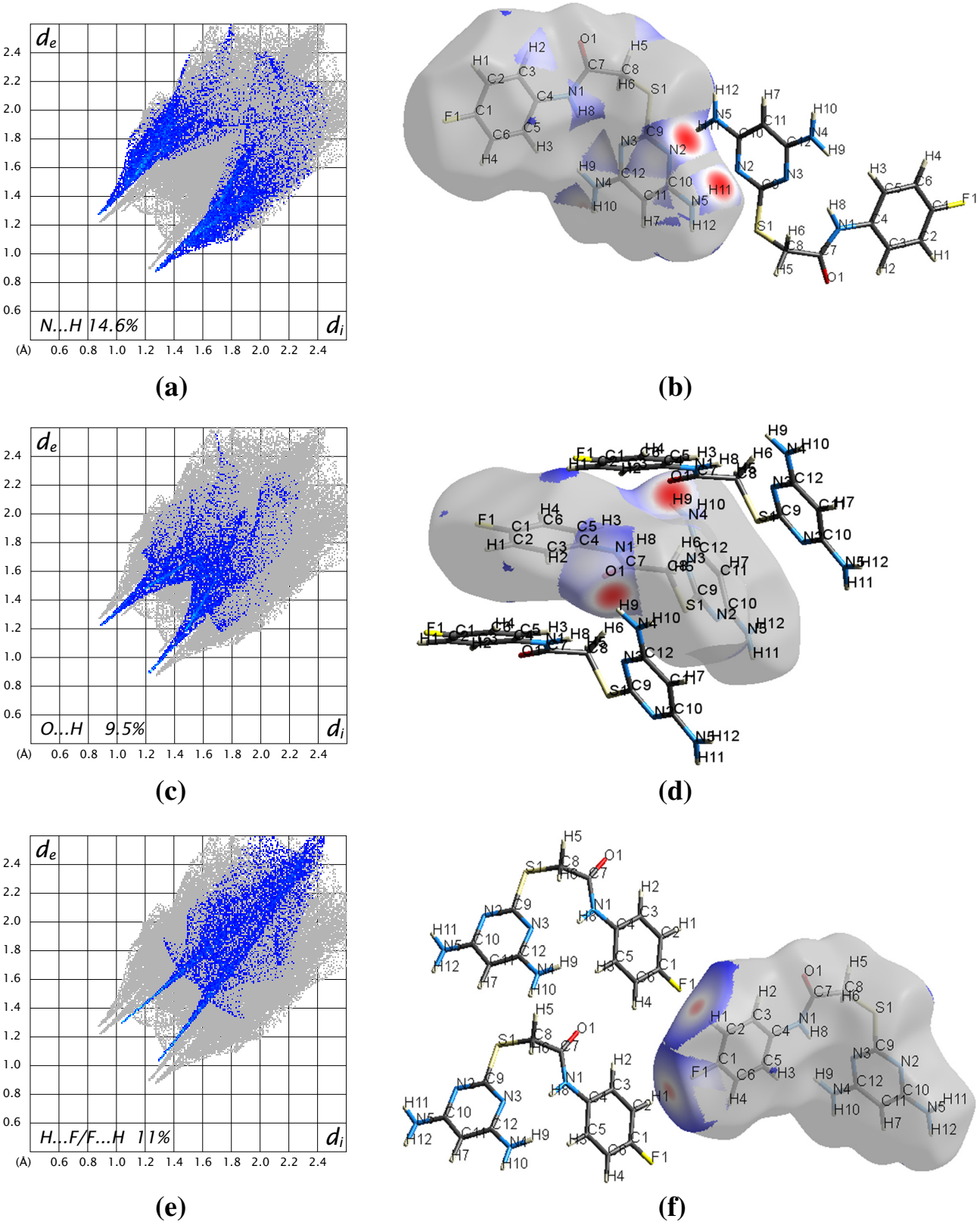

Fig. 3. 2D Fingerprint plot of DAPF mapped over d_{norm} surface showing the characteristic hydrogen bonded interactions. (a) 2D Fingerprint plot of DAPF with characteristic N···H interaction. (b) d_{norm} surfaces of DAPF displaying N···H interaction. (c) 2D Fingerprint plot of DAPF with characteristic O···H interaction. (d) d_{norm} surfaces of DAPF displaying O···H interaction. (e) Fingerprint plot of DAPF with characteristic H ···F interaction. (f) d_{norm} surfaces of DAPF displaying H ···F interaction.

Table 5
Vibrational assignments of DAPF dimer by normal coordinate analysis.

νIR	νRaman	ν(scaled)	$IR_{(I)}$	Raman(I)	Assignments of modes with PED≥10%
3459s		3549	29	70	$\nu_{as}NH_{(Am3)}$(99)
3282s		3279	371	380	$\nu NH_{(Amd)}$(99)
3184s		3208	2993	2	$\nu ssNH_{(Am2)}$ (32)+$\nu ssNH_{(Am4)}$ (32)+$\nu asNH_{(Am3)}$ (16),$\nu asNH_{(Am4)}$ (16)
	3102w	3112	6	44	νCH (99)
3098s	3078s	3093	6	43	νCH(99)
	3035w	3045	6	162	νCH (99)
	3004s	3014	5	80	νCH (99)
2943m		3005	0	71	νMet_{ip}(95)
	2944s	2942	4	110	$\nu ssMet_{(M1)}$(95)
		1670	238	48	νCO(67)+βCNH$_{(Amdr1)}$ (15)
1658s	1663s	1668	266	36	νCO(72) + βCNH$_{(Amdr3)}$ (11)
	1608s	1619	1	13	γNH$_{(Am2)}$ (42)+γNH$_{(Am4)}$ (42)
1602s		1609	848	0	γNH$_{(Am2)}$ (35)+γNH$_{(Am4)}$ (31)+νCN$_{r2}$ (11)
	1576m	1572	28	101	νCC(51)+βCCH(10)+βCNH(10)
1558s		1564	150	13	νCC(26)+νCN(21)+ γNH$_{(Am2)}$)((17)
1508s	1544s	1510	1183	2	νCC(33)+νCN(19)+βCCH(10)
		1507	148	27	νCN $_{(r2)}$ (29)+νCC_{r3} (29)
1470s	1508m	1492	176	21	νCC(31)+νCN$_{(r2)}$((30)
		1479	305	33	βCCH$_{(r1)}$((54)+νCC$_{(r1)}$((31)
	1460m	1412	323	31	βCCH$_{(r1)}$((51)+νCC$_{(r2)}$ (34)
1403s		1410	116	1	νCN$_{(r2)}$((33)+νCNar(30)
	1406m	1341	13	14	νCN$_{(r4)}$((35)+νCNar$_{(r2)}$(28)
1302s	1329s	1326	41	13	γMet_{M2} (90)
		1295	52	13	γMet_{M1}(86)
	1294w	1271	25	6	βCCH$_{(r1)}$(80)
1232m	1240m	1237	6	10	βCCH1$_{(r3)}$(82)
		1190	4	7	νCN$_{(r2)}$ (51)+νCC(11)+ γCNH2 (10)
	1155w	1148	40	15	νCN$_{(r4)}$ (20)+νCC(20)+Rtrd$_{(r3}$ (17)+βCCH$_{(r2)}$ (15)+βCCH$_{(r2)}$ (15)
1130m		1134	22	21	βCCH$_{(r1)}$ (65)+νCC(19)+νCF$_{(r1)}$ (11)
		1129	19	12	βCCH$_{(r3)}$ (66)+νCC$_{(r3)}$ (16)+ νCF$_{(r3)}$(8)
1013m	1129w	1035	15	13	ωCS$_{(M2)}$ (29)+2ωCC3$_{(M1)}$((28)+νCC(10)
		976	56	0	ρCNH$_{(Am2)}$((27)+ ρCNH$_{(Am1)}$ (15)+ρ$_{(Am4)}$ (13)+νCC$_{(M1)}$ (20)
	976m	957	18	29	νCNar4 (45)+Rtrdr4 (37)
		947	20	30	νCNr2 (43)+Rtrdr2(42)ρ
930w	933m	930	0	0	ωCH$_{(r1)}$ (89)
		904	3	3	νCC$_{(r3)}$ (34)+βCN3 (15)+βCN$_{(Amd2)}$ (14)+νCN$_{(r1)}$ (10)
	896m	852	42	23	νCS$_{(M1)}$ (24)+Rasd2' (20)+νCN$_{(r2)}$ (19)+νCC$_{(r1)}$ (15)
838m	849w	832	3	30	νCC$_{(r1)}$ (30)+ ρMet$_{(M1)}$((20)+βCN$_{(Amd)}$ (11)
806m		803	39	1	ωCH$_{(r1)}$(73)
		791	17	7	ωCH$_{(r1)}$((46)+ ρMet$_{(M1)}$((23)
	793w	720	40	0	2ωCH$_{(r1)}$(81)
669m	698w	669	7	7	Rpuk(r2) (27)+ωCN(16)+ωCS(13)
		636	34	1	2ωMet$_{(M1)}$) (32)+2ωCN$_{(M1)}$(23)
618m	632w	622	0	5	Rad$_{(r1)}$ (52)+Rad'$_{(r1)}$ (22)
		591	4	2	Rad'$_{(r3)}$ (20)+ Rad $_{(r3)}$ (19)
518w	588m	533	3	17	ωCS$_{(M2)}$ (31)+ Rad2'$_{(M2)}$(15)+ νCN $_{(r4)}$ (10)
		494	32	5	ω$_{(Amd2)}$ (20)+ νCS$_{(M2)}$(19)+ Rad'$_{(M2)}$ (13)
	495w	449	1	5	βCN$_{(r2)}$ (18)+βNNr2 (16)+Rad$_{(r2)}$ (14)
	432w	402	10	7	βNCC$_{(M2)}$ (30)+ τCC(15)+ Rad'$_{(r2)}$(11)
	393w	381	1	0	Rayt$_{(r3)}$ (56)+ ωCH$_{(M2)}$ (21)+ Rat1'$_{(r3)}$ (15)
	362w	326	5	3	Rpuk$_{(r4)}$ (15)+ωCF$_{(M2)}$ (12)
	322w	298	7	4	βNN$_{(r2)}$ (37)+βCN$_{(r2)}$ (16)
	284w	234	7	2	βCN$_{(r1)}$ (32)+βCN$_{(r3)}$ (21)+βCF$_{(r3)}$ (11)
	229w		2	1	τSCM2 (21)+ Rayt$_{(r4)}$ (19)+τCC$_{(M2)}$ (17)

νIR- Frequency of Infrared.
νRaman- Frequency of Raman.
νCal –Calculated frequency.
aIR- Infrared intensity.
bIRaman- Raman intensity.
PED- Potential energy distribution.
s: strong; m: medium; w:weak.
Symbols used: ν -stretching; ν_{as} - asymmetric stretching; ν_{as} - symmetric stretching; β – bending; ω – wagging; γ- inplane bending; γ'- outplane bending; ρ- rocking; τ- torsion; Rad- asymmetric deformation; Rad'- asymmetric deformation out of plane; Rpuk- puckering; Amd - amide; Am -amine; ip – inplane stretching; Met- methyl; M1-moleculeI; M2-moleculeII; r1- ring1; r2- ring2; r3- ring3; r4- ring4.

of the neighbouring pyrimidine ring, which is responsible for the distinctive red spot on the d_{norm} surface as shown in Fig. 3(b). As seen in Fig. 3(c) O···H interaction makes up 9.5% of the Hirshfed surface of the molecule in the structure. The red spot on the d_{norm} surface is due to the interaction of the carbonyl oxygen of the acetamide group with the proton of the diaminopyrimidine Fig. 3(d). It is noteworthy that H···F contributes 11% on the Hirshfeld surface as seen by two sharp peaks Fig. 3(e), is due to the fluorine atom from the phenyl group interacts with hydrogen atom of the neighbouring phenyl group, which is responsible for the red spot on the $d_{norm\ surface}$ as seen in Fig. 3(f). Hirshfeld analysis results shows that prominent interaction has been observed in N···H, than H···F and

H···O. Multiple hydrogen bonding interaction, impart enhanced stability to supramolecular structures.

4.4. Vibrational spectral analysis

The dimer molecule of DAPF consists of 64 atoms, which undergo 186 vibrational modes. The assignments of the fundamental modes of vibrations have been made based on the normal coordinate analysis following the force field calculation with the *ab initio* method used for the geometry optimization of the dimer molecule. Multiple scaling factors have been employed for scaling, and those are available in supplementary Table S3. The vibrational assignments have been carried out on the basis of the characteristic group vibrations of phenyl ring, acetamide group, methylene group, pyrimidine ring and amine group. The experimental and calculated wave numbers of DAPF along with their normal modes and their corresponding potential energy distribution (PED) are presented in Table 5. Experimental and simulated IR and Raman spectra of DAPF have been shown in Figs. 4 and 5.

4.4.1. Phenyl ring vibrations

The vibrations of the disubstituted phenyl ring have been adopted using Wilson's scheme [35]. The C–H stretching frequencies of the disubstituted benzene are expected to be in the region 3000–3100 cm^{-1} [36]. The selection rules allowed for disubstituted benzene for C–H stretching vibrations are 2, 7b, 20a and 20b. The bands observed at 3102 cm^{-1} with medium intensity and the band observed at 3078 cm^{-1} with strong intensity in Raman spectra have been assigned to mode 20b and 2 respectively. The C–H inplane bending vibrations falls in the region 1300 to 1100 cm^{-1} and is characterized by the normal modes 3, 9a, 15, 18a, 18b. The band with weak intensity observed at 1148 cm^{-1} and a strong band at 1130 cm^{-1} in IR have been assigned to mode 18b. The band at 1240cm^{-1} in Raman spectra with weak intensity is assigned to mode 3. The out of plane bending vibrations of the para disubstituted phenyl ring exhibits in the region 1000–675 and the allowed selection rules are 10a, 10b, 17a, 17b. The bands observed at 836, 805 cm^{-1} in IR spectra and Raman bands at 894 cm^{-1}, 933 cm^{-1} have been assigned to modes 10b and 10a respectively.

In the case of disubstituted benzene derivatives the selection rule allows five normal modes for C–C stretching vibrations. The modes are 8a, 8b, 19a, 19b and 14. In Raman spectrum the vibration mode 8a has been observed at 1563 cm^{-1} and 1544 cm^{-1} and in simulated spectrum it has been observed at 1572 cm^{-1} and 1545 cm^{-1}. The ring mode appears at 1470 cm^{-1} in the IR spectrum and the corresponding calculated wavenumber is 1492 cm^{-1}. The counterpart Raman band has been observed at 1463 cm^{-1} and the theoretical band at 1479 cm^{-1}. The radial skeletal mode 6a of the phenyl ring has been observed at 808 cm^{-1} in IR and Raman. The simulated IR band observed at 805 cm^{-1} and the Raman band at 795 cm^{-1} has been assigned to mode 6a. The outofplane skeletal mode 4 has been observed at 674 cm^{-1} in IR spectrum and at 670 cm^{-1} in simulated IR spectrum.

4.4.2. Amide group vibrations

Amides are of fundamental chemical interest owing to their conjugation between lone pair electrons in the Nitrogen and the carbonyl bond results in distinct physical and chemical properties [37]. Secondary amides are probably the most important as they are the backbone of every protein molecule. Secondary amide contains only one N—H stretching band in the infrared spectrum. This band appears between 3370 and 3500 cm^{-1} [38]. Therefore, band observed at 3282 cm^{-1} in IR is assigned to the N—H stretching. The down shift in N–H stretching frequency validates the spectral evidence of the N–H···N intramolecular hydrogen bond formation. The strength of N–H···N bond has been well reflected by an increase in the bond length (0.001 Å). Also, the shift has been evinced by the intramolecular charge transfer interaction between N25 → N12–H13 in NBO basis with the stabilization energy 7.31 kcal/mol. An interesting feature of the amide group is the amide I band and is known as the C═O stretching mode. In fluorophenylacetamide the amide I band arises due to the delocalization of the nitrogen lone pair electrons and is observed as a strong intense band at 1658 cm^{-1} in IR. Normal Coordinate analysis of DAPF shows amide I band has been coupled with amide II and amide III bands. The amide II band known as N–H inplane bending has been observed as an intense peak in the IR spectra at 1515 cm^{-1}. The Raman counterpart is observed at 1519 cm^{-1}. The C═O out of plane bending known as amide VI band has been observed at 518 cm^{-1} in IR and at 525 cm^{-1} in Raman.

4.4.3. Methylene vibrations

The asymmetric and the symmetric vibrations of the methylene group normally occur in the region 3100–2900 cm^{-1} [39]. The presence of the neighbouring acetamide moiety and the sulphur lone pair affects the spectral behaviour of the sp^3 methylene group. The occurrence of the adjacent sulphur atom can shift the position and the intensity of the CH stretching and bending vibrations. The hyperconjugative interactions between the *s* lone pair and σ*(C–H), lowers the wavenumber and the weakening of C–H bonds. NBO result substantiates the above fact as seen from the hyperconjugative interaction S19 → C16–H18 with the stabilization energy of 1.72 kJ/mol. The IR band observed at 2942 $cm^{-1}$with medium intensity is assigned to CH_2 symmetric and asymmetric stretching.

4.4.4. Pyrimidine ring vibrations

Pyrimidine ring vibrations have been characterized by the C–N stretching vibration, C–C stretching and bending vibrations. In pyrimidine, quadrant stretch bands occur at 1590–1520 cm^{-1} [40,41] and the semicircle bands occur in the region 1480–1375 cm-1. These bands can be viewed both in IR spectra as well as Raman spectra [42,43]. The spectrum of DAPF shows the band with strong intensity at 1558 cm-1in IR and the band at 1544 cm^{-1} in Raman with medium intensity have been assigned to quadrant stretching mode. Semicircle stretching vibrations has been observed at 1507 cm^{-1} in IR and Raman spectra. Quadrant inplane bending mode has been observed at 632 cm^{-1} in Raman spectra and the theoretical band at 636 cm^{-1}.

4.4.5. Amine vibrations

In primary amines, vibrational frequencies have been characterized by NH2 antisymmetric stretching, NH2 symmetric stretching, NH2 scissoring, NH2 wagging, C–N stretching and CCN bending. Strong absorption in the range 3548–3459 cm-1 has been marked as NH2 antisymmetric stretching in the IR spectra [44]. In DAPF, the antisymmetric N–H stretching mode has been observed at 3459 cm^{-1} as an intense band in the IR spectrum. The dimer molecule of DAPF has been bonded by two strong N–H···N bonds. In case of primary aromatic amines the symmetric stretching is expected in the region 3422–3360 cm^{-1} [45]. The band observed at 3183 cm^{-1} in IR spectra has been assigned to N–H symmetric stretching. The red shift in wavenumber (~180 cm-1) shows the spectral evidence for the formation of N–H···N intermolecular interactions. This has been validated from the results of optimized geometry as seen with an increase in the N30–H31 bond length by 0.018 Å and the C22–N30–H31 bond angle by 5° over the isolated molecule. Also, the down shift in stretching frequency has been substantiated by the second order perturbation energy that takes place between n1(N53) → σ* (N30–H31) with the stabilization energy of 10.54 kcal/mol and the occupancy of the interacting NBOs. These hydrogen bonded interactions restrain protein molecules to their native configurations and an important role in inhibiting the gelling of sickle–cell deoxyhemoglobin. Also, intermolecular N···H–N hydrogen bonding plays an important role in the stability of protein structure [46]. The NH_2 scissoring mode in aryl amine is in the region of 1638–1602 cm^{-1} [47,48]. The NH_2 scissoring mode known as the symmetric deformation mode is assigned to the band at 1622 cm^{-1}in the IR while the respective Raman band is observed at 1608 cm^{-1}.

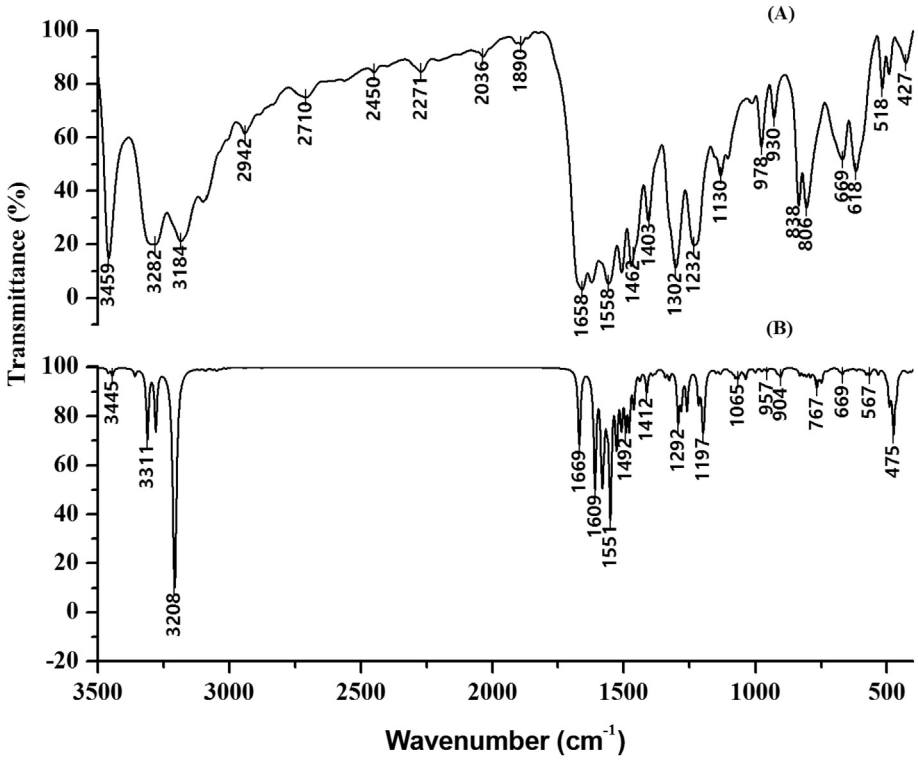

Fig. 4. FT-IR spectrum of DAPF. (A) Experimental Fourier transform-Infrared spectra of DAPF revealing the characteristics Infrared bands in the region 4000–0 cm^{-1}. (B) Simulated Fourier transform-Infrared spectra of DAPF revealing the characteristics Infrared bands in the region 4000 cm^{-1} to 400 cm^{-1}.

Raman bands with weak intensity at 698 $cm^{-1}$and the widened IR band at 669 cm-1contributes to the NH_2 wagging mode. The band observed with medium intensity at 1446 $cm^{-1}$and 1406 cm^{-1}have been assigned to the C–N stretching vibration in IR and Raman respectively.

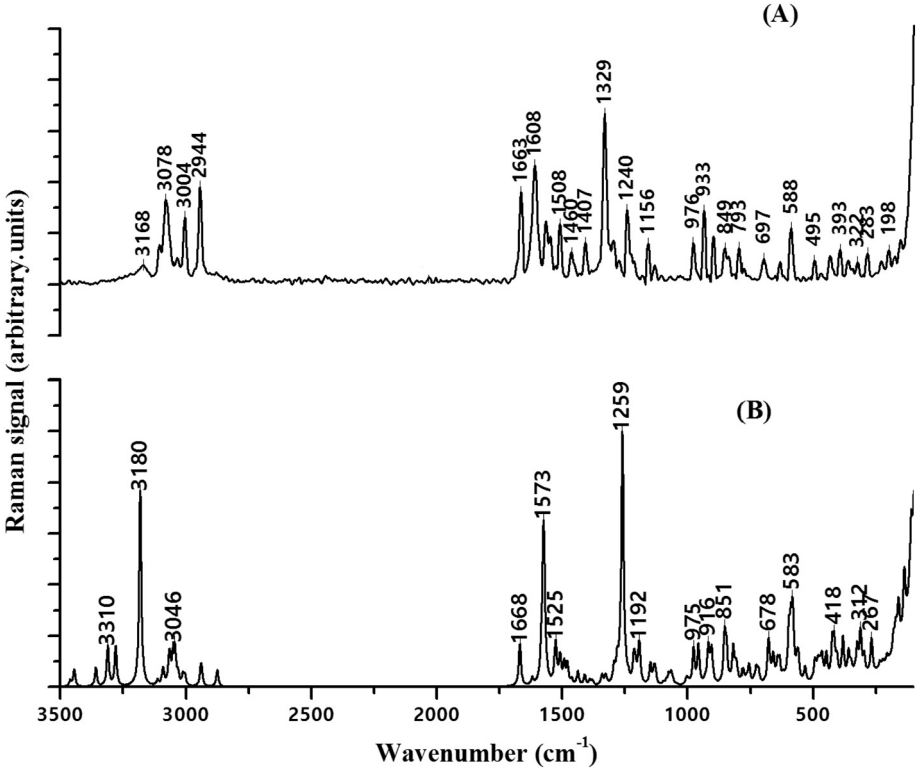

Fig. 5. FT-Raman spectrum of DAPF. (a) Experimental Fourier transform-Raman spectra of DAPF revealing the characteristics Raman bands in the region 4000 cm^{-1} to 0 cm^{-1}. (b) Simulated Fourier transform-Raman spectra of DAPF revealing the characteristics Raman bands in the region 4000 cm^{-1} to 0 cm^{-1}.

4.5. Drug likeness of DAPF

According to the rule of thumb, orally absorbed drugs tend to obey Lipinski's rule of five. The rule of five was derived from an analysis of compounds from the World Drugs Index database aimed at identifying features that have been important in making a drug orally active. It has been found that the factors concerned involved numbers that are multiples of five: a molecular weight less than 500; no more than 5 hydrogen bond donor (HBD) groups; no more than 10 hydrogen bond acceptor groups; a calculated log *P* value less than +5 [49–54]. DAPF has been passed through Lipinski's rule of five (Table 6) to overcome drug-likeness filter.

4.6. ADMET property analysis

There is an overall of 26 constraints in ADMET statistics, which has been taken from the full text of peer-reviewed scientific journals through weekly PubMed and Google Scholar searches from 2002 to 2011 [55]. ADMET (Absorption, Distribution, Metabolism, Excretion and Toxicity) results show that DAPF (+) in human intestinal absorption and blood-brain barrier permeability, which suggests that the molecule is well absorbed in the human body (Table 7). Inhibition and initiation of P-glycoprotein have been described as the causes of drug-drug interactions. [56]. It has been observed that DAPF has P-glycoprotein non-inhibitor, which shows the noninteracting activity of DAPF with other drugs. ADMET data show DAPF is in permissible limit [55,57]. Organic cation transporters are accountable for drug absorption and disposition in the kidney, liver, and intestine [58]. ADMET result of DAPF shows that it has been a non-inhibitor of renal organic cation transporter. The human cytochromes P450 (CYPs) are responsible for about 90% oxidative metabolic reactions. Inhibition of CYP enzymes will lead to inductive or inhibitory failure of drug metabolism [59]. A non-inhibitor and non-Substrate property of DAPF supports the fact it is safe to the human liver. The Ames test is employed to test the mutagenic activity of chemical compounds. It is usually carried out to test bacteria and viruses to whether a given chemical can cause cancer [60,61]. ADMET result of DAPF is shown in Table 7.

ADMET result shows DAPF has been non-ames toxic and non-carcinogenic. Human Ether-à-go-go-Related Gene (hERG) is a gene delicate to drug binding [62]. ADMET results shows DAPF have been weak inhibitor and non-inhibitor of hERG inhibition (predictor I and II). That means the DAPF molecules will well bind with SARS-CoV-2 main protease [63]. Analyzing the ADMET properties, together with their attributes and prediction, has given an idea about the pharmacokinetic properties of DAPF.

4.7. Docking study of DAPF with SARS-CoV-2 main protease

4.7.1. In silico calculation

Molecular docking has been used to acquire binding modes and binding affinities of DAPF. Binding mode and affinity to SARS-CoV-2 main protease are essential for *insilico* drug design [64–68]. The protein structure of SARS-COV-2 has been retrieved from protein data bank (PDB id: 5r80). The protein (SARS-COV-2) and ligands (DAPF) structures have been modified by Autodock Tools [69]. The chains of main protease have been modified by removing water and bound ligand. Missing amino acids have been checked and polar hydrogens have been added to the protein structure. Center Grid box x:5.108, y:18.9177, z:-18.1863 and number of points in x,y,z dimensions are considered as 30x30x30 $Å^3$ respectively and grid spacing has been taken as 0.3750 Å. Ligand has been prepared by adding Gasteiger charges, detecting root and choosing torsions from the torsion tree of Autodock Tools panel [70]. Docking procedure has been performed by using the Lamarckian genetic algorithm [71] and the results have been tabulated in Table 8.

DAPF bound to the active site of main protease with good complementarity (Fig. 6) and formed three hydrogen bonds and four hydrophobic bonds with the mainprotease. The binding energy of the

Table 6
Drug likeness properties of DAPF.

Lipinski's rule	Drug likeness properties of DAPF	Lipinski's rule satisfied (yes/no)
Molecular weight (≤500 g/mol)	293.32 g/mol	Yes
Number of HB acceptors (≤10)	4	Yes
Number of HB donors (≤5)	3	Yes
Lipophilicity log P (≤5)	1.74	Yes
Molar refractivity (40 to130)	76	Yes

Table 7
Absorption, distribution, metabolism, excretion, toxicity (ADMET) properties of DAPF.

Model	Result	Probability
Absorption		
Blood-brain barrier	BBB+	0.9789
Human intestinal absorption	HIA+	0.8629
Caco-2 permeability	Caco2-	0.5649
P-glycoprotein substrate	Non-substrate	0.7566
P-glycoprotein inhibitor	Non-inhibitor	0.6319
	Non-inhibitor	0.9546
Renal organic cation transporter	Non-inhibitor	0.7981
Distribution		
Subcellular localization	Mitochondria	0.4296
Metabolism		
CYP450 2C9 substrate	Non-substrate	0.8784
CYP450 2D6 substrate	Non-substrate	0.8302
CYP450 3A4 substrate	Non-substrate	0.6196
CYP450 1A2 inhibitor	Inhibitor	0.7502
CYP450 2C9 inhibitor	Inhibitor	0.5890
CYP450 2D6 inhibitor	Non-inhibitor	0.6972
CYP450 2C19 inhibitor	Inhibitor	0.6940
CYP450 3A4 inhibitor	Inhibitor	0.6666
CYP Inhibitory promiscuity	High CYP Inhibitory Promiscuity	0.8737
Excretion		
Toxicity		
Human ether-a-go-go-related gene inhibition	Weak inhibitor	0.9943
	Non-inhibitor	0.7087
AMES toxicity	Non AMES toxic	0.6974
Carcinogens	Non-carcinogens	0.8358
Fish toxicity	Low FHMT	0.8744
Tetrahymena pyriformis toxicity	High TPT	0.7894
Honey bee toxicity	Low HBT	0.8417
Biodegradation	Not ready biodegradable	1.0000
Acute oral toxicity	III	0.5613
Carcinogenicity (three-class)	Non-required	0.4045

Table 8
Bond distances of DAPF and types of bond with SARS-CoV-2 main protease.

Molecule name DAPF	Distance (Å)	Bond category	Bond type
DAPF:H - A:LEU141:O	1.77679	Hydrogen bond	Conventional hydrogen bond
A:ARG188:HA - : DAPF:F	2.62388	Hydrogen bond; Halogen	Carbon hydrogen bond; Halogen (fluorine)
DAPF:H - A:HIS164:O	2.9894	Hydrogen bond	Conventional hydrogen bond
A:ASP187:O - :DAPF:F	3.16325	Halogen	Halogen (fluorine)
DAPF:F - A:MET49	4.28188	Hydrophobic	Alkyl
DAPF - A:MET49	4.65914	Hydrophobic	Pi-alkyl
DAPF - A:CYS145	4.69418	Hydrophobic	Pi-alkyl
A:HIS41 - :DAPF	4.74499	Hydrophobic	Pi-Pi stacked
A:MET165:SD - :DAPF	5.50755	Other	Pi-sulphur

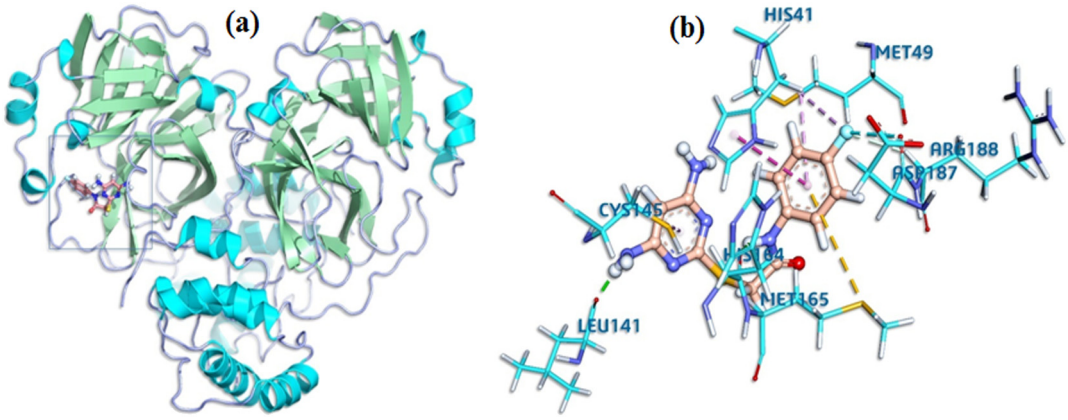

Fig. 6. Comprehensive perception of main protease and DAPF after docking, (a) secondary structure of SARS-CoV-2 mainprotease represented by ribbon and DAPF represented is by ball and stick model (b) interactions of DAPF with SARS-CoV-2 main protease amino acids. Bonds are in dots. DAPF (orange) surrounding amino acids (sky blue) are in three letters code.

nonbonding interaction is −8.7 kcal/mol. All these results present a clear view that DAPF can irreversibly interact with main protease. The catalytic dyad composed of Histidine 41 and Cysteine 145 is a set of amino acids that can be found in the active site of most SARS-CoV-2 main proteases, plays an essential role in drug binding [72]. DAPF bound both to Histidine 41 and Cysteine 145 (Fig. 6 and Table 8) claims to be a good antiviral drug.

5. Conclusion

The compound DAPF has been characterized by FT-IR, FT-Raman at B3LYP/6-311++G(d,p) level using DFT calculations and the complete vibrational analysis has been carried out in order to elucidate the structure activity relationship. The presence of the intermolecular and intramolecular hydrogen bonds has been analyzed using NBO analysis. The transfer of electrons from the lone pair nitrogen to the anti-bonding orbital of N—H bond evinces the formation of two hydrogen bonds that brings about most interesting biological properties. The occurrence of N–H···N intermolecular interactions and the conspicuous shifting in the wavenumber have been authenticated by the increase in N—H bond length and an increase in the electron density in the antibonding orbitals. Also, intermolecular N- H···N hydrogen bonding plays an important role in the stability of protein structure. Hirshfeld surfaces and the 2D fingerprint plot confirms the presence of the intermolecular contacts N- H···N, C- H···O, C- H···F and their quantitative contributions, impart stability to the system. Drug likeness and ADMET property analysis gives an idea about the pharmacokinetic properties of the title molecule. The binding energy −8.7 kcal/mol of the nonbonding interaction presents a clear view that DAPF can irreversibly interact with SARS-CoV-2 protease.

CRediT authorship contribution statement

Jenepha Mary: Conceptualization, Data Curation, Investigation, Software, writing and Validation. Mohd Usman Mohd Siddique, Venkatesan Jayaprakash: Provision of Sample. Sayantan Pradhan: Writing and Data Curation. James. C: Supervision.

Declaration of competing interest

The authors declare that they have no known competing financial interests or personal relationships that could have appeared to influence the work reported in this paper.

Appendix A. Supplementary data

Supplementary data to this article can be found online at https://doi.org/10.1016/j.saa.2020.118825.

References

[1] R. Mohd, H. Asif, S. Mohammad, M. Ravinesh, H. Afzal, A. Obaid, Design and synthesis of pyrimidine molecules endowed with thiazolidin-4-one as new anticancer agents, Eur. J.Med.Chem 83 (2014) 630–645, https://doi.org/10.1021/jm0009540.
[2] R.E. Hester, R.B. Girling, Spectroscopy of Biological Molecules, Royal Society of Chemistry, London, UK, 1991https://doi.org/10.1002/9783527615438.refs.
[3] R. Diwakar, C. Wenmin, T. Ye, C. Xuwang, Z. Peng, D. Clercq, E. Pannecouque, L. Xinyong, Design, synthesis and biological evaluation of 3-benzyloxy-linked pyrimidinylphenylamine derivatives as potent HIV-1 NNRTIs, Bioorg. & Med. Chem 21 (2013) 7398–7405, https://doi.org/10.1016/j.bmc.2013.09.051.
[4] Q.-Y. Wang, S.J. Patel, E. Vangrevelinghe, H.Y. Xu, R. Rao, O. Heudi, N.L. Ma, M.K. Poh, W.Y. Phong, T.H. Keller, E. Jacoby, S.G. Vasudevan, Antimicrob. Agents And Chemother (2009, May) 1823–1831, https://doi.org/10.1128/aac.01148-08.
[5] Joanne Philp, Brian G. Lawhorn, Alan P. Graves, 4,6-Diaminopyrimidines as highly preferred troponin I-interacting kinase (TNNI3K), J. Med. Chem. 61 (2018) 3076–3088, https://doi.org/10.1021/acs.jmedchem.8b00125.
[6] Venkat R. Gadhachanda, et al., 4-Aminopyrimidines as novel HIV-1 inhibitors, Bioorg. Med. Chem. Lett. 17 (2007) 260–265, https://doi.org/10.1016/j.bmcl.2006.09.047.
[7] E.P. Aparna, K.S. Devaky, Advances in the solid-phase synthesis of pyrimidine derivatives, ACS Comb. Sci. 21 (2) (2019) 35–68, https://doi.org/10.1021/acscombsci.8b00172.
[8] A. Turck, N. Ple, F. Mongin, G. Queguiner, Advances in the directed metallation of azines and diazines (pyridines, pyrimidines, pyrazines, pyridazines, quinolines, benzodiazines and carbolines), Part. 2:metallation of pyrimidines,pyrazines, pyridazines and benzodiazines, Tetrahedron 57 (21) (2001) 4489–4505, https://doi.org/10.1016/S0040-4020(01)00225-3.
[9] J.M. Schomaker, T.J. Delia, Arylation of halogenated pyrimidines via a Suzuki coupling reaction, J. Org. Chem. 66 (21) (2001) 7125–7128, https://doi.org/10.1021/jo010573+.
[10] V. Krishnakumar, R. John Xavier, Molecular and vibrational structure of 2-mercapto pyrimidine and 2,4-diamino-6-hydroxy-5-nitroso pyrimidine: FT-IR, FT-Raman and quantum chemical calculations, Spectrochim. ActaA 63 (2006) 454–463, https://doi.org/10.1016/j.saa.2005.05.031.
[11] S. Gunasekaran, U. Ponnambalam, S. Muthu, Vibrational and normal coordinate analysis of pyrazinamide, Asain Journal of Chemistry 16 (3) (2004) 1513–1518.
[12] W.J. McCarthy, L. Lapinski, M.J. Novak, L. Adamovicz, Out-of-plane vibrations of NH2 in 2-aminopyrimidine and formamide, J. Chem. Phys. 108 (24) (1998) 10116–10128, https://doi.org/10.1063/1.476471.
[13] P. Politzer, G.P. Kirschenheuter, R.S. Miller, Computational study of 2-aminopyrimidine, 2-amino-5-nitropyrimidine, and the corresponding S,S-dimethyl-N-sulfilimines, J. Phys. Chem. 92 (1988) 1436, https://doi.org/10.1021/j100317a015.
[14] S. Seshadri, S. Gunasekaran, S. Muthu, S. Kumaresan, R. Arunbalaji, Vibrational spectroscopy investigation using ab initio and density functional theory on flucytosine, J. Raman Spectrosc. 38 (2007)1523–1531. doi:https://doi.org/10.1002/jrs.1808.
[15] S. Muthu, J. Uma Maheswari, Quantum mechanical study and spectroscopic (FT-IR, FT-Raman, 13C, 1H, UV) study, first order hyperpolarizability, NBO analysis, HOMO and LUMO analysis of 4-[(4-aminobenzene) sulfonyl] aniline by ab initio HF and density functional method, Spectrochim. ActaA 92 (2012) 154–163, https://doi.org/10.1016/j.saa.2012.02.056.
[16] A.Y. Khan, M.B. Kalashetti, N.S. Belavagi, N. Deshapa-nde, I.A.M. Khazi, Synthesis, characterization and biological evaluation of novel thienopyrimidine and triazolothienopyrimidine derivatives as anti-tubercular and antibacterial agents, Med. Chem. Res. 23 (2014) 3235–3243, https://doi.org/10.1007/s00044-013-0900-1.
[17] Subasri, Timiri Ajay Kumar, Barij Nayan Sinha, Venkatesan Jayaprakash, Vijayan Viswanathan and Devadasan Velmurugana. Crystal Structures of *N*-(4-chlorophen-yl)-2-[(4,6-di-amino-pyrimidin-2-yl)sulfan-yl]acetamide and *N*-(3-chlorophen-yl)-2-[(4,6-di-amino-pyrimidin-2-yl)sulfan-yl]acetamide, Acta Cryst E 73 (2017) 467–471. doi:https://doi.org/10.1107/s2056989017003243.

[18] Carolin Hoyera, Angelika Alonsoa, Beate Schlotter-Weigelb, Michael Plattena, Marc Fatara, HIV-associated cerebellar dysfunction and improvement with aminopyridine therapy, Case Rep Neurol 9 (2017) 121–126 10.1159%2F000475544.

[19] B.M. Johnson, Y.Z. Shu, X. Zhuo, N.A. Meanwell, Metabolic and pharmaceutical aspects of fluorinated compounds, J. Med. Chem. (2020)https://doi.org/10.1021/acs.jmedchem.9b01877.

[20] M.J. Frisch, G.W. Trucks, H.B. Schlegel, G.E. Scuseria, M.A. Robb, J.R. Cheeseman, G. Scalmani, V. Barone, G.A. Petersson, H. Nakatsuji, X. Li, M. Caricato, A. Marenich, J. Bloino, B.G. Janesko, R. Gomperts, B. Mennucci, H.P. Hratchian, J.V. Ortiz, A.F. Izmaylov, J.L. Sonnenberg, D. Williams-Young, F. Ding, F. Lipparini, F. Egidi, J. Goings, B. Peng, A. Petrone, T. Henderson, D. Ranasinghe, V.G. Zakrzewski, J. Gao, N. Rega, G. Zheng, W. Liang, M. Hada, M. Ehara, K. Toyota, R. Fukuda, J. Hasegawa, M. Ishida, T. Nakajima, Y. Honda, O. Kitao, H. Nakai, T. Vreven, K. Throssell, J.A. Montgomery Jr., J.E. Peralta, F. Ogliaro, M. Bearpark, J.J. Heyd, E. Brothers, K.N. Kudin, V.N. Staroverov, T. Keith, R. Kobayashi, J. Normand, K. Raghavachari, A. Rendell, J.C. Burant, S.S. Iyengar, J. Tomasi, M. Cossi, J.M. Millam, M. Klene, C. Adamo, R. Cammi, J.W. Ochterski, R.L. Martin, K. Morokuma, O. Farkas, J.B. Foresman, D.J. Fox, Gaussian 09. Revision C.01, Gaussian, Inc., Wallingford CT, 2009.

[21] E.D. Glendening, A.E. Reed, J.E. Carpenter, F. Weinhold, NBO Version 3.1, TCI, University of Wisconsin, Madison, 1998.

[22] T. Sundius, Scaling of ab initio force fields by MOLVIB, Vib. Spectrosc 29 (2002) 89–95, https://doi.org/10.1016/S0924-2031(01)00189-8.

[23] T. Sundius, Molvib - a flexible program for force field calculations, J. Mol. Struct. 218 (1990) 321–326, https://doi.org/10.1016/0022-2860(90)80287-T.

[24] P. Pulay, G. Fogarasi, G. Pongor, J.E. Boggs, A. Vargha, Combination of theoretical ab initio and experimental information to obtain reliable harmonic force constants, J. Am. Chem. Soc. 105 (1983) 7037, https://doi.org/10.1021/ja00362a005.

[25] S.K. Wolff, D.J. Grimwood, J.J. McKinnon, M.J. Turner, D. Jayatilaka, M.A. Spackman, CrystalExplorer (Version 3.0), [prod.], University of Western Australia, 2012.

[26] J.J. McKinnon, D. Jayatilaka, M.A. Spackman, Towards quantitative analysis of intermolecular interactions with Hirshfeld surfaces, Chem. Commun. (2007) 3814–3816, https://doi.org/10.1039/b704980c.

[27] G.M. Morris, D.S. Goodsell, R.S. Halliday, R. Huey, W.E. Hart, R.K. Belew, A.J. Olson, Automated docking using a lamarckian genetic algorithm and empirical binding free energy function, J. Comput. Chem. 19 (1998) 1639–1662, https://doi.org/10.1002/(SICI)1096-987X(19981115)19:14%3C1639.

[28] The PYMOL Molecular Graphics System, LLC, Schrodinger2009.

[29] X. Li, L. Liu, H. Schlegel, Bernhard, on the physical origin of blue-shifted hydrogen bonds, J. Am. Chem. Soc. 124 (2002) 9639–9647, https://doi.org/10.1021/ja020213j.

[30] E.D. Glendening, A.E. Reed, J.E. Carpenter, F. Weinhold, NBO Version 3.1, Gaussian Inc., Pittsburgh, 2003.

[31] A.E. Reed, L.A. Curtis, F.A. Weinhold, Intermolecular interactions from a natural bond orbital, donor-acceptor viewpoint, Chem. Rev. 88 (1988) 899–926, https://doi.org/10.1021/cr00088a005.

[32] J. Bernstein, R.E. Davis, L. Shimoni, Chang, Patterns in hydrogen bonding: functionality and graph set analysis in crystals, Angew. Chem. Int. Ed. Engl. 34 (15) (1995) 1555–1573, https://doi.org/10.1002/anie.199515551.

[33] F.L. Hirshfeld, Bonded-atom fragments for describing molecular charge densities, Theoreticachimica Acta 44 (2) (1977) 129–138, https://doi.org/10.1002/anie.199515551.

[34] M.A. Spackman, D. Jayatilaka, Hirshfeld surface analysis, CrystEngComm 11 (2009) 19–32, https://doi.org/10.1039/B818330A.

[35] G. Varsanyi, Assignments for Vibrational Spectra of 700 Benzene Derivatives; Adam Hilger: London, 1974.Fersht, A. Enzyme Structure and Mechanism, Freeman, New York, 1985https://ui.adsabs.harvard.edu/link_gateway/1975JMoSt..29..383B/doi:10.1016/0022-2860(75)85047-2.

[36] G. Socrates, Infrared Characteristic Group Frequencies, Wiley–Interscience Publication, New York, 1980.

[37] Brian C. Smith, Infrared Spectral Interpretation: A Systematic Approach, CRC Press, 1998.

[38] D. Lin–Vien, N.B. Colthup, W.G. Fately, J.G. Grasselli, F.F. Bentley, The Handbook of Infrared and Raman Characteristic Frequencies of Organic Molecules, Academic, New York, 1991.

[39] I. Hubert Joe, G. Aruldhas, S.A. Kumar, P. Ramasamy, Vibrational spectra and phase transition in triglycine sulpho-phosphate, J. Cryst. Res.Technol. 29 (1994) 685–692, https://doi.org/10.1002/crat.2170290520.

[40] F. Dollish, G. Fately, W.G. Bentley, Characteristic Raman Frequencies of *Organic* Compounds, John Wiley & Sons, New York, 1974.

[41] S.K. Freeman, Applications of Laser Raman Spectroscopy, John Wiley and Sons, New York, 1974https://doi.org/10.1016/0022-2860(75)80089-5.

[42] K.H. Michaelian, S.M. Ziegler, Vibrational spectra and assignments for series of mono- and dihalonaphthalenes, Appl. Spectrosc. 27 (1973) 13–21 10.1366%2F000370273774333966.

[43] L.N. Short, H.W. Thompson, Infra-red spectra of derivatives of pyrimidine, J. Chem. Soc. 38 (1952) 168–187, https://doi.org/10.1039/JR9520000168.

[44] Brian C. Smith, Infrared Spectral Interpretation: A Systematic Approach, CRC Press, 2011.

[45] R.A. Nyquist, Factors affecting infrared group frequencies: carbonyl stretching absorption bands, sadtler, Appl. Spectrosc. 40 (3) (1986) 336–339 10.1366%2F0003702864509105.

[46] G.A. Jeffrey, W. Saenger, Hydrogen Bonding in Biological Structures, New York, Springer-Verlag, 1991https://doi.org/10.1007/978-3-642-85135-3_1.

[47] T. Rajamani, S. Muthu, M. Karabacak, Electronic absorption, vibrational spectra, nonlinear optical properties, NBO analysis and thermodynamic properties of N-(4-nitro-2-phenoxyphenyl) methanesulfonamide molecule by ab initio HF and density functional methods, Spectrochim. ActaA 108 (2013)https://doi.org/10.1016/j.saa.2013.01.090.

[48] Daimay Lin-Vien, Norman Colthup, William Fateley, F.F. Bentley, Infrared and Raman characteristics Frequencies of Organic Compounds, Academic Press, Jeanette Grasselli, 1991.

[49] C.A. Lipinski, Lead-and drug-like compounds: the rule-of-five revolution, Drug Discov. Today Technol. 1 (4) (2004) 337–341, https://doi.org/10.1016/j.ddtec.2004.11.007.

[50] W.P. Walters, M.A. Murcko, Prediction of drug-likeness, Adv. Drug Deliv. Rev. 54 (3) (2002) 255–271, https://doi.org/10.1016/s0169-409x(02)00003-0.

[51] D.E. Clark, S.D. Pickett, Computational methods for the prediction of drug-likeness, Drug Discov. Today 5 (2) (2000) 49–58, https://doi.org/10.1016/s1359-6446(99)01451-8.

[52] S. Tian, J. Wang, Y. Li, Li, L. Xu, T. Hou, The application of in silico drug-likeness predictions in pharmaceutical research, Advanced drug delivery reviews 86 (2015) 2–10, https://doi.org/10.1016/j.addr.2015.01.009.

[53] O. Ursu, A. Rayan, A. Goldblum, T. Oprea, Understanding drug-likeness, Wiley Interdiscip. Rev. Comput. Mol. Sci 5 (2011) 760–781, https://doi.org/10.1002/wcms.52.

[54] W.J. Egan, W.P. Walters, M.A. Murcko, Guiding molecules towards drug-likeness, Current Opinion in Drug Discovery & Development. 5 (4) (2002) 540–549.

[55] Feixiong Cheng, Weihua Li, Yadi Zhou, Jie Shen, Zengrui Wu, Guixia Liu, Philip W. Lee, Yun Tang, admetSAR: a comprehensive source and free tool for assessment of chemical ADMET properties, J. Chem. Inf. Mode 52 (11) (2012)https://doi.org/10.1021/ci300367a 3099-3015.

[56] S. Soga, H. Shirai, M. Kobori, Hirayama, Use of amino acid composition to predict ligand-binding sites, J. Chem. Inf. Model. 47 (2) (2007) 400–406, https://doi.org/10.1021/ci6002202.

[57] L. Escuder-Gilabert, M. Molero-Monfort, R.M. Villanueva-Camañas, S. Sagrado, M.J. Medina-Hernández, Potential of biopartitioning micellar chromatography as an in vitro technique for predicting drug penetration across the blood–brain barrier, J. Chromatogr. B 807 (2004) 193–201, https://doi.org/10.1016/j.jchromb.2004.04.004.

[58] L. Zhang, C.M. Brett, Giacomini KMJArop, toxicology, role of organic cation transporters in drug absorption and elimination, Annu. Rev. Pharmacol. Toxicol. 38 (1) (1998) 431–460, https://doi.org/10.1146/annurev.pharmtox.38.1.431.

[59] Vinita Uttamsingh, Chuang Lu, Gerald Miwa, Liang-Shang Gan, Relative contributions of the five major human cytochromes P450, 1A2, 2C9, 2C19, 2D6, and 3A4, to the hepatic metabolism of the proteasome inhibitor bortezomib, Drug Metab. Dispos. 33 (11) (2005) 1723–1728, https://doi.org/10.1124/dmd.105.005710.

[60] D. Forman, Ames, the Ames test, and the causes of cancer, BMJ 303 (6800) (1991) 428–429 10.1136%2Fbmj.303.6800.428.

[61] K. Mortelmans, Zeiger EJMrf, mutagenesis mmo, The Ames Salmonella/microsome mutagenicity assay. Mutation Research 455 (2000) 29–60, https://doi.org/10.1016/s0027-5107(00)00064-6.

[62] M.C. Sanguinetti, M.J.N. Tristani-Firouzi, hERG potassium channels and cardiac arrhythmia, Nature 440 (7083) (2006) 463–4699, https://doi.org/10.1038/nature04710.

[63] W. Dai, B. Zhang, H. Su, J. Li, Y. Zhao, X. Xie, Z. Jin, F. Liu, C. Li, Y. Li, F. Bai, Structure-based design of antiviral drug candidates targeting the SARS-CoV-2 main protease, Science 368 (6497) (2020 Apr 22) 1331–1335, https://doi.org/10.1126/science.abb4489.

[64] G.M. Morris, M., Lim-Wilby, Molecular docking, InMolecularmodeling of proteins Humana Press, chapter 19 (2008) 365–382, https://doi.org/10.1007/978-1-59745-177-2_19.

[65] N. Brooijmans, Kuntz ID, Molecular recognition and docking algorithms, Annu. Rev. Biophys. 32 (1) (2003) 335–373, https://doi.org/10.1146/annurev.biophys.32.110601.142532.

[66] B.K. Shoichet, S.L. Mc Govern, B. Wei, J.J. Irwin, Lead discovery using molecular docking, Current opinion in chemical biology 6 (4) (2002) 439–446, https://doi.org/10.1016/s1367-5931(02)00339-3.

[67] G. Jones, P. Willett, Glen RC, Leach AR, R. Taylor, Development and validation of a genetic algorithm for flexible docking, J. Mol. Biol. 267 (3) (1997) 727–748, https://doi.org/10.1006/jmbi.1996.0897.

[68] R.D. Taylor, P.J. Jewsbury, J.W. Essex, A review of protein-small molecule docking methods, J. Comput. Aided Mol. Des. 16 (3) (2002) 151–166, https://doi.org/10.1023/a:1020155510718.

[69] G.M. Morris, R. Huey, W. Lindstrom, M.F. Sanner, R.K. Belew, D.S. Goodsell, A.J. Olson, AutoDock4 and AutoDockTools4: automated docking with selective receptor flexibility, J. Comput. Chem 16 (2009) 2785–2791, https://doi.org/10.1002/jcc.21256.

[70] J. Gasteiger, M. Marsili, Iterative partial equalization of orbital electronegativity-a rapid access to atomic charges, Tetrahedron. 36 (22) (1980) 3219–3228, https://doi.org/10.1016/0040-4020(80)80168-2.

[71] G.M. Morris, D.S. Goodsell, R.S. Halliday, R. Huey, W.E. Hart, R.K. Belew, A.J. Olson, Automated docking using a Lamarckian genetic algorithm and an empirical binding free energy function, J. Comput. Chem. 19 (14) (1998) 1639–1662, https://doi.org/10.1002/(SICI)1096-987X(19981115)19:14%3C1639::AID-JCC10%3E3.0.CO;2-B.

[72] A.R. Buller, C.A. Townsend, Intrinsic evolutionary constraints on protease structure, enzyme acylation, and the identity of the catalytic triad, Proc. Natl. Acad. Sci. 110 (8) (2013) E653–E661, https://doi.org/10.1073/pnas.1221050110.